Nuclear magnetic resonance parameters of atomic xenon dissolved in Gay-Berne model liquid crystal

Juho Lintuvuori,* Michal Straka, and Juha Vaara†
Laboratory of Physical Chemistry, Department of Chemistry, University of Helsinki, P.O. Box 55 (A.I. Virtasen aukio 1), FIN-00014 Helsinki, Finland
(Received 23 October 2006; published 21 March 2007)

We present constant-pressure Monte Carlo simulations of nuclear magnetic resonance (NMR) spectral parameters, nuclear magnetic shielding relative to the free atom as well as nuclear quadrupole coupling, for atomic xenon dissolved in a model thermotropic liquid crystal. The solvent is described by Gay-Berne (GB) molecules with parametrization $\kappa=4.4$, $\kappa'=20.0$, and $\mu=\nu=1$. The reduced pressure of $P^{\star}=2.0$ is used. Previous simulations of a pure GB system with this parametrization have shown that upon lowering the temperature, the model exhibits isotropic, nematic, smectic-*A*, and smectic-*B*/molecular crystal phases. We introduce spherical xenon solutes and adjust the energy and length scales of the GB-Xe interaction to those of the GB-GB interaction. This is done through first principles quantum chemical calculations carried out for a dimer of model mesogens as well as the mesogen-xenon complex. We preparametrize quantum chemically the Xe nuclear shielding and quadrupole coupling tensors when interacting with the model mesogen, and use the parametrization in a pairwise additive fashion in the analysis of the simulation. We present the temperature evolution of $^{129/131}$Xe shielding and ^{131}Xe quadrupole coupling in the different phases of the GB model. From the simulations, separate isotropic and anisotropic contributions to the experimentally available total shielding can be obtained. At the experimentally relevant concentration, the presence of the xenon atoms does not significantly affect the phase behavior as compared to the pure GB model. The simulations reproduce many of the characteristic experimental features of Xe NMR in real thermotropic LCs: Discontinuity in the value or trends of the shielding and quadrupole coupling at the nematic-isotropic and smectic-*A*–nematic phase transitions, nonlinear shift evolution in the nematic phase reflecting the behavior of the orientational order parameter, and decreasing shift in the smectic-*A* phase. The last observation is due to the preference of the xenon solutes to occupy the interlayer space where the density of the medium is reduced as compared to the layers. There are systematic deviations, however, in the magnitude of the shielding and its discontinuities, as well as the distribution of the solutes in the translationally ordered smectic-*A* phase, between the simulation and experiment. These deficiencies are believed to result from the lack of flexibility of the GB model.

DOI: 10.1103/PhysRevE.75.031707 PACS number(s): 61.30.Cz, 32.30.Dx, 33.25.+k, 82.20.Wt

I. INTRODUCTION

Guest noble gas atoms are used as inert agents in nuclear magnetic resonance (NMR) studies of various host media such as liquids, liquid crystals (LCs), micro- and mesoporous solids, and solid surfaces [1–3]. In particular, the structure and dynamics of thermotropic LCs have been widely investigated through the NMR spectra of dissolved ^{129}Xe and ^{131}Xe, due to the sensitivity of the electron cloud and, hence, the spectral parameters of the Xe atom to the physical properties of its surroundings [4]. The possibility of increasing the signal-to-noise ratio by several orders of magnitude by optical pumping procedures [5,6] makes xenon particularly attractive in materials research.

Intermolecular interaction-induced effects on the NMR observables, nuclear magnetic shielding of the ^{129}Xe and ^{131}Xe nuclei and/or the quadrupole coupling of the ^{131}Xe nucleus in atomic xenon, have been studied with a range of computational methods, e.g., in Refs. [7–15]. In order to investigate systems complex enough to render explicit electronic structure modeling inapplicable for all the relevant instantaneous configurations, preparametrized pairwise additive models have been developed [7–10,14]. In such models the isotropic Xe NMR chemical shift is calculated as a sum of pair interactions with the atoms defining the environment. The pair interactions are *a priori* parametrized in terms of the atomic positions by quantum chemical calculations of suitable, small model systems, and are used without further electronic structure work when analyzing positional information contained in a simulation trajectory. The method is in complete analogy to molecular simulation using empirical, preparametrized force fields.

The LC phases pose significant computational demands for modeling the NMR of dissolved xenon, and atomistic solvent models can hardly be used due to the large number of LC molecules necessary. A solution is to adopt a coarse-grained, nonatomistic description of the medium [16]. A further complication arises due to the fact that not only isotropic but also tensorial properties of the NMR interactions need to be preparametrized, as their effect is included in the spectra taken in LC mesophases [4]. In such systems, the molecules do not tumble isotropically but are partially oriented with respect to the optical axis (director) $\boldsymbol{n}$. In the case of thermotropic LCs, temperature can be used to control the existence

*Present address: Department of Chemistry, University of Durham, United Kingdom.
†Author to whom correspondence should be addressed. Electronic address: juha.t.vaara@helsinki.fi

and degree of orientational and positional order, and these are delicately reflected in the temperature evolution of the NMR parameters of guest Xe atoms [4].

In the present paper we build a simulation model for studying the distribution and NMR parameters of atomic solutes, Xe to start with, in thermotropic LC phases, using the constant-pressure Monte Carlo technique [17] and a coarse-grained LC model. A widely used one-site potential to mimic LC interactions is the Gay-Berne (GB) model [18,19]. Its four parameters κ, κ', μ, and ν control the anisotropy of the attractive and repulsive intermolecular interactions. It has been shown [20,21] that, e.g., for the parametrization GB (κ=4.4, κ'=20.0, μ=1, ν=1) at the reduced pressure of $P^{\star}$=2.0, the model produces the following succession of phases upon reducing the temperature: isotropic (I), nematic (N), smectic-A (Sm-A), and smectic-B(Sm-B)/molecular crystal (Cr). Hence, the model is suitable for comparison with experimental data taken from solutions exhibiting a rather rich phase behavior. We introduce atomic solutes by adopting a potential model for the interaction between a GB and a Lennard-Jones particle [22,23]. The energy and range parameters of the model are adapted specifically for xenon solutes, by first principles quantum chemical calculations of the complex of xenon atom and a model mesogen on the one hand, and of the dimer of the model mesogens on the other hand.

The anisotropic NMR parameters of the solute, $^{129/131}$Xe nuclear shielding tensor relative to that of the free Xe atom, as well as ^{131}Xe quadrupole coupling, are preparametrized through quantum chemical calculations of the complex of the model mesogen and the xenon atom at different relative geometries. The positional information produced in the simulation is analyzed in a pairwise additive model, where the summation of the distinct, anisotropic solute-solvent pair NMR interactions is carried out after transformation from the coordinate frame of each individual GB-Xe pair to the principal axis frame of the instantaneous orientational order tensor $\boldsymbol{Q}$, common to all the pairs.

We carry out simulations at an estimated experimental concentration of Xe atoms, in both ascending and descending temperature series covering the phases mentioned above. The energetic and structural properties are averaged and compared to those of the pure GB model [20,21] in the present parametrization. The Xe NMR properties are calculated and broken into their isotropic and anisotropic contributions, and a comparison is made with the experimental findings for specific LC solutions [24,25].

II. THEORY

A. Liquid crystal solvent

The GB model is used to describe the interaction between two rigid particles with axial symmetry [19]. The particle i is assigned with the center of mass vector $\boldsymbol{r}_i$ and the orientation $\hat{\boldsymbol{u}}_i$ of its rotational symmetry axis. The interaction energy between the GB particles i and j can be written as

$$\mathcal{U}_{ij}^{\mathrm{GB}}(\boldsymbol{r}_{ij},\hat{\boldsymbol{u}}_i,\hat{\boldsymbol{u}}_j) = 4\epsilon(\hat{\boldsymbol{r}}_{ij},\hat{\boldsymbol{u}}_i,\hat{\boldsymbol{u}}_j)\left[\left(\frac{\sigma_0}{R_{ij}}\right)^{12} - \left(\frac{\sigma_0}{R_{ij}}\right)^{6}\right], \quad (1)$$

where the anisotropic interparticle distance parameter reads

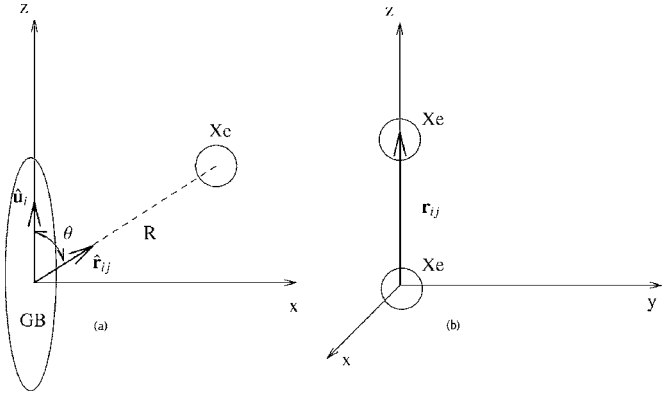

FIG. 1. Local coordinate frame for interacting (a) Gay-Berne particle-xenon (GB-Xe) and (b) xenon dimer (Xe-Xe) systems.

$$R_{ij} = r_{ij} - \sigma(\hat{\boldsymbol{r}}_{ij},\hat{\boldsymbol{u}}_i,\hat{\boldsymbol{u}}_j) + \sigma_0. \quad (2)$$

σ_0 denotes the smallest molecular diameter, i.e., the contact distance in the cross configuration of the two particles. The simulations are carried out in the reduced unit system where this parameter is assigned the value of one. Vector $\boldsymbol{r}_{ij}$ is the vector between the centers of mass of the molecules i and j, and $\hat{\boldsymbol{r}}_{ij}$ is the corresponding unit vector. The contact distance $\sigma(\hat{\boldsymbol{r}}_{ij},\hat{\boldsymbol{u}}_i,\hat{\boldsymbol{u}}_j)$ and the potential strength $\epsilon(\hat{\boldsymbol{r}}_{ij},\hat{\boldsymbol{u}}_i,\hat{\boldsymbol{u}}_j)$ depend on the relative orientations of the molecular long axes $\hat{\boldsymbol{u}}_i$ and $\hat{\boldsymbol{u}}_j$, as well as $\hat{\boldsymbol{r}}_{ij}$. σ and ϵ are also dependent on the molecular length to breadth ratio κ and the ratio of the potential well depths in the parallel side-by-side and end-to-end configurations, κ'. In addition, the potential strength has two more anisotropy parameters, μ and ν. These four parameters completely specify a given GB potential model denoted as GB(κ,κ',μ,ν). The explicit functional forms of σ and ϵ can be found in the original paper by Gay and Berne [19].

B. Solute interactions

For the interaction between the GB molecule i and a spherical xenon atom j [22,23],

$$\mathcal{U}_{ij}^{\text{GB-Xe}}(\boldsymbol{r}_{ij},\hat{\boldsymbol{u}}_i) = 4\epsilon(\hat{\boldsymbol{r}}_{ij},\hat{\boldsymbol{u}}_i)\left[\left(\frac{\sigma_0^{\text{GB-Xe}}}{R_{ij}}\right)^{12} - \left(\frac{\sigma_0^{\text{GB-Xe}}}{R_{ij}}\right)^{6}\right] \quad (3)$$

was used, with the anisotropic distance and range parameters defined this time as

$$R_{ij} = r_{ij} - \sigma(\hat{\boldsymbol{r}}_{ij},\hat{\boldsymbol{u}}_i) + \sigma_0^{\text{GB-Xe}}, \quad (4)$$

$$\sigma(\hat{\boldsymbol{r}}_{ij},\hat{\boldsymbol{u}}_i) = \sigma_0^{\text{GB-Xe}}[1-\chi(\hat{\boldsymbol{r}}_{ij}\cdot\hat{\boldsymbol{u}}_i)^2]^{-1/2} = \sigma_0^{\text{GB-Xe}}(1-\chi\cos^2\theta)^{-1/2}. \quad (5)$$

θ is the angle between the long axis of the GB molecule and the vector $\boldsymbol{r}_{ij}$ between the two particles, as illustrated in Fig. 1(a).

As compared to the pure GB model, allowing the LC molecules to interact with spherical solutes introduces modified geometrical parameters: the contact distance in the side (s, with θ=90°) configuration $\sigma_0^{\text{GB-Xe}}$, as well as the ratio

σ_e/σ_s of the contact distances in the configurations where the spherical atom is at the end (e, with $\theta=0°$) and on the side of the GB particle, appearing in

$$\chi = 1 - \left(\frac{\sigma_e}{\sigma_s}\right)^{-2}. \tag{6}$$

The function determining the depth of the potential well takes the form

$$\epsilon(\hat{\boldsymbol{r}}_{ij},\hat{\boldsymbol{u}}_i) = \epsilon_0^{\text{GB-Xe}}[1-\chi'(\hat{\boldsymbol{r}}_{ij}\cdot\hat{\boldsymbol{u}}_i)^2]^{\mu} = \epsilon_0^{\text{GB-Xe}}(1-\chi'\cos^2\theta)^{\mu},$$

$$\chi' = 1 - \left(\frac{\epsilon_e}{\epsilon_s}\right)^{1/\mu}, \tag{7}$$

where the energy parameter $\epsilon_0^{\text{GB-Xe}}$ differs from ϵ_0 in the GB-GB interaction (the latter is assigned the value of one in the reduced unit system). ϵ_e/ϵ_s is the ratio of the potential energy minima in the end and side configurations, and μ controls the anisotropy of the interaction at intermediate values of θ.

For the interaction between the spherical solute atoms, the ordinary Lennard-Jones potential

$$\mathcal{U}_{ij}^{\text{Xe-Xe}}(r_{ij}) = 4\epsilon_0^{\text{Xe-Xe}}\left[\left(\frac{\sigma_0^{\text{Xe-Xe}}}{r_{ij}}\right)^{12} - \left(\frac{\sigma_0^{\text{Xe-Xe}}}{r_{ij}}\right)^{6}\right] \tag{8}$$

was used.

C. Nuclear magnetic resonance parameters of the solute

1. Pair interaction contributions to nuclear shielding

In the local coordinate system of Fig. 1(a), the GB-Xe contribution to the $^{129/131}$Xe nuclear shielding tensor from the interaction of the xenon solute with one LC molecule, $\boldsymbol{\sigma}-\sigma_{\text{free}}\mathbf{1}$, follows the C_s point group site symmetry with reflection in the xz plane. Here, σ_{free} is the isotropic shielding constant of the free Xe atom and $\mathbf{1}$ is the 3×3 unit matrix. This interaction-induced contribution takes the form

$$\boldsymbol{\sigma}_{\text{GB-Xe}} = \begin{pmatrix} \sigma_{xx} & 0 & \sigma_{xz} \\ 0 & \sigma_{yy} & 0 \\ \sigma_{zx} & 0 & \sigma_{zz} \end{pmatrix}, \tag{9}$$

with the tensor components parametrized as

$$\sigma_{xx} = \sigma_{xx}^{s}(R)\sin^2\theta + \sigma_{\perp}^{e}(R)\cos^2\theta,$$

$$\sigma_{yy} = \sigma_{\perp}^{e}(R),$$

$$\sigma_{zz} = \sigma_{\parallel}^{s}(R)\sin^2\theta,$$

$$\sigma_{xz} = \sigma_{xz}(R)\sin\theta\cos\theta,$$

$$\sigma_{zx} = \sigma_{zx}(R)\sin\theta\cos\theta. \tag{10}$$

We present the argument leading to this parametrization in the auxiliary material [26,27]. This leaves five functions to be determined via quantum chemical calculations, $\sigma_{xx}^{s}(R)$, $\sigma_{\perp}^{e}(R)$, $\sigma_{\parallel}^{s}(R)$, $\sigma_{xz}(R)$, and $\sigma_{zx}(R)$, where the superscripts e and s refer to the end and side configurations of the GB-Xe pair, respectively. The subscripts $\perp$ and $\parallel$ denote the direction perpendicular to (in the e configuration) and parallel with the long axis of the GB particle, in the corresponding order.

At the low solute concentration of our simulation, the direct Xe-Xe interactions only play a minor role. For completeness, we parametrize the Xe-Xe contribution for the Xe shielding tensor as

$$\boldsymbol{\sigma}_{\text{Xe-Xe}} = \begin{pmatrix} \sigma_{\perp} & 0 & 0 \\ 0 & \sigma_{\perp} & 0 \\ 0 & 0 & \sigma_{\parallel} \end{pmatrix} \tag{11}$$

in the local coordinate frame of Fig. 1(b). The form of the tensor is appropriate to the axial $C_{\infty v}$ site symmetry of the Xe nucleus, and the components $\sigma_{\parallel}$ and $\sigma_{\perp}$ can be parametrized as functions of the internuclear distance r in terms of the isotropic shielding constant $\sigma(r)$ and the shielding anisotropy $\Delta\sigma(r)$ (with respect to the direction of the internuclear axis) as

$$\sigma_{\perp} = \sigma(r) - \tfrac{1}{3}\Delta\sigma(r),$$

$$\sigma = \sigma(r) + \tfrac{2}{3}\Delta\sigma(r). \tag{12}$$

$\sigma_{\parallel}$ is practically zero similarly as $\sigma_{\parallel}^{e}$ for the GB-Xe shielding interaction [27,28].

2. Pair interaction contributions to quadrupole coupling

The parametrization of the ^{131}Xe nuclear quadrupole coupling tensor $\boldsymbol{\chi}_{\text{GB-Xe}}$ follows the procedure outlined for shielding, with the following exceptions. First, $\boldsymbol{\chi}$ is a symmetric and traceless tensor, and these properties limit the number of independent, nonvanishing tensor components as components to $\boldsymbol{\sigma}$. Second, quadrupole coupling has a nonzero $\chi_{\parallel}^{e}$ component also in the axially symmetric "end" configuration, unlike the shielding tensor. Finally, in a free xenon atom the quadrupole coupling vanishes due the spherical symmetry of the electron cloud, and consequently the interaction with the solvent determines all of quadrupole coupling.

Altogether the GB-Xe contribution to the ^{131}Xe quadrupole coupling takes in the local coordinate frame the form

$$\boldsymbol{\chi}_{\text{GB-Xe}} = \begin{pmatrix} \chi_{xx} & 0 & \chi_{xz} \\ 0 & -(\chi_{xx}+\chi_{zz}) & 0 \\ \chi_{xz} & 0 & \chi_{zz} \end{pmatrix}, \tag{13}$$

where we define the components as

$$\chi_{xx} = \chi_{xx}^{s}(R)\sin^2\theta - \tfrac{1}{2}\chi_{\parallel}^{e}(R)\cos^2\theta,$$

$$\chi_{zz} = \chi_{\parallel}^{s}(R)\sin^2\theta + \chi_{\parallel}^{e}(R)\cos^2\theta,$$

$$\chi_{xz} = \chi_{xz}(R)\sin\theta\cos\theta. \tag{14}$$

We have employed the fact that $\chi_{\perp}^{e} = -\frac{1}{2}\chi_{\parallel}^{e}$ in the $C_{\infty v}$ end configuration, due to the tracelessness of $\boldsymbol{\chi}$. This leaves the following four functions to be parametrized quantum chemically, $\chi_{xx}^{s}(R)$, $\chi_{\parallel}^{e}(R)$, $\chi_{\parallel}^{s}(R)$, and $\chi_{xz}(R)$.

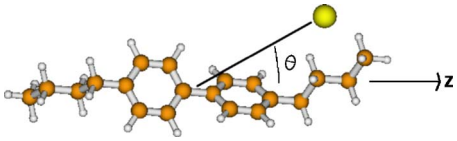

FIG. 2. (Color online) Atomistic model liquid crystal molecule used to parametrize the interaction between a liquid crystal molecule and Xe atom.

For the Xe-Xe contribution one obtains in the coordinate frame of Fig. 1(b),

$$\boldsymbol{\chi}_{\text{Xe-Xe}} = \begin{pmatrix} -\frac{1}{2}\chi_{zz} & 0 & 0 \\ 0 & -\frac{1}{2}\chi_{zz} & 0 \\ 0 & 0 & \chi_{zz} \end{pmatrix}. \tag{15}$$

III. COMPUTATIONAL METHODS

A. Quantum chemical parametrization

1. Interaction energy

The potential energy surface of the GB-Xe interaction was determined quantum chemically using an atomistic model of a generic LC molecule, and letting it interact with a Xe atom in different spatial configurations. The model LC molecule (Fig. 2) consists of a biphenyl core part and two saturated hydrocarbon tails of four carbon atoms, in the all-*trans* configuration. The proportions of the model are consistent with the length-to-distance ratio of 4.4 characteristic of the present GB parametrization. The absence of strong local electric dipole moments in the model corresponds to a GB particle experiencing only anisotropic repulsion-dispersion interactions, not decorated by electrostatic multipoles.

The model was geometry optimized [29] at the three-parameter hybrid B3LYP [30] density-functional theory (DFT) and 6-311++G** basis set [31] level using the Gaussian 03 program [32]. The principal axis corresponding to the smallest eigenvalue of the moment of inertia tensor of the molecule was associated with the z direction of the local coordinate system of the interacting GB-Xe pair [Fig. 1(a)]. The potential $V^{\text{LC-Xe}}$ was calculated at the resolution-of-identity second-order Møller-Plesset perturbation theory (RI-MP2) [33] level using the default doubly polarized valence triple-zeta (def-TZVPP) [34] basis set, on the Turbomole program [35]. The Stuttgart energy-consistent relativistic pseudopotential [36] was employed for the Xe atom. The calculations were corrected by the counterpoise (CP) method [37] to reduce the basis set superposition error.

The position of the Xe atom with respect to the LC model molecule was selected at different distances from the coordinate origin (placed at the midpoint of the bond between the two phenyl rings), at the following polar angles: $\theta=0°$, 30°, and 90°. To obtain a parametrization reflecting the rotational symmetry of the GB model, calculations at the latter two values of θ were carried out at values of the azimuthal angle ϕ picked in 60° intervals, after which a thermal (Boltzmannian) average of the interaction potential at different ϕ was approximated as

TABLE I. Parameters of the potential energy function of the interaction between Gay-Berne particle and xenon solute.

Parameter	Value	Unit
$\sigma_0^{\text{GB-Xe}}$	3.6	Å
$\epsilon_0^{\text{GB-Xe}}$	105.57	meV
σ_e/σ_s	3.32	
ϵ_e/ϵ_s	0.16	
μ	0.35	
σ_0[a]	4.5	Å
ϵ_0[a]	157.58	meV

[a]Parameters of the interaction between Gay-Berne particles.

$$V^{\text{LC-Xe}}(r,\theta) = \frac{\sum_{i=1}^{6} V^{\text{LC-Xe}}(r,\theta,\phi_i)\exp[-V^{\text{LC-Xe}}(r,\theta,\phi_i)/kT]}{\sum_{i=1}^{6} \exp[-V^{\text{LC-Xe}}(r,\theta,\phi_i)/kT]},$$

$$\phi_i = i \times 60° \tag{16}$$

at $T=300$ K, following the idea presented in Ref. [38].

The parameters $\sigma_0^{\text{GB-Xe}}$, σ_e/σ_s, $\epsilon_0^{\text{GB-Xe}}$, and ϵ_e/ϵ_s of the GB-Xe interaction were least-squares fitted to the LC-Xe interaction with $\theta=0°$ and $\theta=90°$, the latter averaged over the azimuthal angle as in Eq. (16). The potential anisotropy parameter μ does not affect the shape of the potential in the end and side configurations, but was manually adjusted to reproduce the RI-MP2 data at the intermediate angle, $V^{\text{LC-Xe}}(r,\theta=30°)$. The resulting GB-Xe potential parameters are listed in Table I.

Finally, to place the GB-Xe interaction to the energy and length scale appropriate to the GB-GB interaction, a parallel dimer of the model LC molecule of Fig. 2 was investigated at the same level of theory as the LC-Xe interaction, RI-MP2. The potential energy $V^{\text{LC-LC}}(r,\theta=90°,\phi_1=i\times 60°,\phi_2=j\times 60°)$ (with $i,j=1,2,\ldots,6$) was subjected to a Boltzmann averaging at $T=300$ K in a fashion analogous to that of Eq. (16), except that double sums involving the azimuthal angles $\phi_i^{1,2}$ of the two molecules were used. The resulting effective potential $V^{\text{LC-LC}}(r)$ was fitted to the Morse potential form [39], and the numerical values of ϵ_0 and σ_0 were extracted based on the depth of the potential minimum and the distance at which the $V^{\text{LC-LC}}$ curve crosses zero, respectively. For the unit energy, the value of $\epsilon_0=157.58$ meV was obtained, which is considerably higher than the value of 22.8 meV proposed by Bates and Luckhurst [20]. For the length scale, $\sigma_0=4.5$ Å was obtained, which is the same value as suggested in Ref. [20]. The GB-Xe potential is illustrated in the auxiliary material [26].

For the Xe-Xe interaction we adopted the van der Waals radius of Xe, $\sigma_0^{\text{Xe-Xe}}=4.32$ Å [40], and the best available *ab initio* quantum chemical value for the potential well depth in the Xe dimer, $\epsilon_0^{\text{Xe-Xe}}=24.40$ meV [15].

TABLE II. Parameters of $^{129/131}$Xe nuclear magnetic resonance shielding and ^{131}Xe quadrupole coupling tensors when interacting with the model liquid crystal.[a]

Parameter	A	$p_{A,0}$	$p_{A,1}$	$p_{A,2}$	$p_{A,3}$
$\sigma^s_{xx}(R)$	$-1.2026297065\times10^{1}$	3.3134189498×10^{0}	9.0507886417×10^{0}	$-1.6025243568\times10^{0}$	
$\sigma^e_{\perp}(R)$	$-1.1672648797\times10^{1}$	$3.9997702047\times10^{-2}$	1.1636011366×10^{1}	$-1.5288591743\times10^{0}$	$-3.4266848087\times10^{-1}$
$\sigma^s_{\parallel}(R)$	$-5.2671604883\times10^{1}$	4.5165162489×10^{0}	1.5171022733×10^{1}	$-2.3590723634\times10^{1}$	9.9306821259×10^{0}
$\sigma_{xz}(R)$	3.1228263091×10^{1}	5.3141730331×10^{0}	$6.6334674074\times10^{-1}$		
$\sigma_{zx}(R)$	3.3141615175×10^{1}	4.8095621340×10^{0}	$7.0308516233\times10^{-1}$		
$\chi^s_{xx}(R)$	2.9222586183×10^{0}	3.2835741349×10^{0}	3.6896880124×10^{0}	$-6.4687585514\times10^{-1}$	
$\chi^e_{\parallel}(R)$	$-5.2004492490\times10^{-1}$	1.6846133021×10^{1}	$-1.0664334268\times10^{1}$	2.3313944890×10^{0}	
$\chi^s_{\parallel}(R)$	$-3.8213603446\times10^{-1}$	9.9725303666×10^{0}	$-5.2124031847\times10^{0}$	$-6.8656465241\times10^{-1}$	$6.8925841175\times10^{-1}$
$\chi_{xz}(R)$	$-7.6955322406\times10^{-6}$	$-3.8558980871\times10^{1}$	$-3.4192991767\times10^{1}$	2.8627512246×10^{1}	
Parameter	B	$p_{B,0}$	$p_{B,1}$	$p_{B,2}$	$p_{B,3}$
$\chi^e_{\parallel}(R)$	$2.9010256384\times10^{-1}$	2.6871761243×10^{1}	$-4.6117061897\times10^{1}$	3.7140396050×10^{1}	
$\chi_{xz}(R)$	1.3445614681×10^{0}	6.5490556256×10^{1}	$-1.7162263010\times10^{2}$	1.2463647343×10^{2}	

[a]The unit of A and B is ppm in the case of $^{129/131}$Xe shielding and MHz for ^{131}Xe quadrupole coupling. The p_i are in units of σ_0^{-i}.

2. Nuclear magnetic resonance parameters

Studies of, e.g., Xe shielding in the Xe_2 system as a function of the internuclear distance [15], have shown that qualitatively correct behavior (as judged by comparison with high-quality correlated *ab initio* calculations) can be obtained at the uncorrelated Hartree-Fock level of electronic structure theory, where dispersion interaction effects are completely absent. Together with the observed spatial range of the shielding interactions, this points to the emerging consensus [14,41] that the short-range overlap effects dominate the shielding response of noble gases to intermolecular forces. The minor role of dispersion also justifies the use of DFT for such properties [12,13,42].

Presently, the GB-Xe NMR interactions $\sigma^s_{xx}(R)$, etc., were determined at the B3LYP level using the model system of Fig. 1(a) at $\theta=0°$ and 90° (diagonal tensor components) and 30° (the off-diagonal components), on the GAUSSIAN 03 software. The polarized valence triple-zeta (TZVP) [34] basis was used for the carbon and hydrogen atoms. For Xe, the [23*s* 18*p* 15*d* 1*f*/16*s* 14*p* 12*d* 1*f*] set (in the [primitive/contracted] notation) developed for NMR properties in Ref. [15] on the basis of the primitives of Fægri [43], was employed. The CP corrections and thermal averaging over the azimuthal angle at $T=300$ K [as in Eq. (16)] were employed for the individual tensor components, when $\theta=30°$ or 90°. Before averaging, radius vector $\mathbf{r}_{ij}$ (from the LC molecule to the Xe atom) was rotated to the local xz plane, for each studied $\theta=30°$ or 90° configuration.

For the distance dependence of the shielding and coupling tensor components, the following functional form [10] was used:

$$\chi^e_{\parallel}(R) = \frac{A}{R^{p_A(R)}} + \frac{B}{R^{p_B(R)}},$$

$$p_i(R) = p_{i,0} + p_{i,1}R + p_{i,2}R^2 + \cdots + p_{i,n}R^n, \quad i = A,B \tag{17}$$

and similarly for the other functions. As before [10,15], we imply no physical interpretation for this form, but regard it as a convenient way of representing the quantum chemically calculated data. The B term in Eq. (17) is only necessary when the data include a sign change as a function of R. The resulting parameters for the LC-Xe NMR interactions are listed in Table II and illustrated in the auxiliary material [26].

For the NMR interaction appropriate to the Xe-Xe pairs, $\sigma(r)$, $\Delta\sigma(r)$, and $\chi_{zz}(r)$, the *ab initio* coupled-cluster singles and doubles (CCSD) [44] data for Xe_2 by Hanni *et al.* [15] were adopted.

B. Monte Carlo simulations

One of the present authors [45] wrote a program for carrying out Monte Carlo simulations of systems consisting of GB particles and spherical solutes in the isothermal-isobaric (*NPT*) ensemble [46]. Constant pressure simulation is natural choice for systems where translationally ordered phases can be expected. In canonical, constant volume (*NVT*) simulations, such phases may fail to be naturally commensurate with the dimensions of the simulation box [47,48], leading to artifacts. Standard periodic boundary conditions [20] were applied with the simulation cell taking the shape of a rectangular box with unequal side lengths. We used the same parametrization GB ($\kappa=4.4$, $\kappa'=20.0$, $\mu=1$, $\nu=1$) as in Refs. [20,21]. The interactions were truncated at $r_c=5.5\sigma_0$ and no long-range corrections were applied. The reduced pressure of $P^\star=2.0$ was used in all simulations. We adopted the Verlet neighbor list [49] with the outer radius of $6.8\sigma_0$ and updates that were performed when the maximum particle displacement in any Cartesian direction exceeded 29% of the difference between the outer radius of the list and the cutoff radius.

The starting configuration for the pure GB system was constructed as described in Ref. [21]. The initial structure was a crystal with six molecular layers parallel to the xy plane, with the long axes of the GB particles arranged in the z direction. A hexagonal in-layer order was adopted in each layer consisting of 15×18 particles, making the total number of particles equal to $N_{GB}=6\times15\times18=1620$. In simula-

tions with spherical solutes, 10 GB particles were replaced with xenon atoms, i.e., $N_{Xe}=10$ and $N_{GB}=1610$. The ratio of N_{Xe} to N_{GB} was deduced from the Xe solubility data in water in normal conditions [50], and assuming that xenon dissolves better in a nonpolar LC solvent than in water, particularly at the elevated pressure appropriate to the experimental conditions [4].

Each simulation cycle consisted of an attempt to both translate and rotate all the N_{GB} molecules and to translate all the N_{Xe} solutes, in turn. The rotations of the GB particles were performed around a random direction by a random angle. We used the Mersenne Twister random number generator [51]. In addition to particle moves, each cycle also included two or three attempts (depending on the state point) to vary the volume of the simulation cell as detailed in Ref. [21]. In short, isotropic volume moves were attempted in the I and N phases that lack long-range translational order, whereas the two simulation cell dimensions perpendicular to $\boldsymbol{n}$ were adjusted isotropically and the dimension along $\boldsymbol{n}$ independently, in the Sm-A phase. Finally, all three side lengths of the cell were held independent in the Cr phase.

Simulations were carried out for a series of both ascending and descending reduced temperatures in the range $T^\star=0.8-1.9$. In both heating and cooling runs, the starting configuration for a certain value of $T^\star$ was adopted from the final state of the previous temperature in the series. In the cooling runs, the crystalline structure was first melted into an isotropic liquid at $T^\star=2.0$, and the resulting configuration was used as the starting point for simulation at $T^\star=1.9$. To achieve speed-up, trivial parallelization was employed by dividing the temperature series into successive, sequentially treated blocks. In another approach resembling the procedures of Refs. [20,21], temperature series was divided into two sequences, each containing every second value of $T^\star$. No difference in the resulting state points should arise between the different methods, provided that a sufficiently long equilibration is carried out.

At each simulated temperature, equilibration runs of at least 75 000 cycles were performed. Close to phase transitions, the system was equilibrated longer, using minimally 150 000 cycles. The maximum rotational-translational displacements were adjusted to achieve a combined acceptance rate of 30%–35%, whereas 25% was used for the box-length fluctuations [21]. These adjustments were performed periodically during the first 40% of the length of the equilibration run at each $T^\star$. The length of the subsequent production runs was 25 000 cycles. The configuration was written to disk after every five simulation cycles.

It has been shown that in mesophases with translational long-range order, equilibration occurs faster if $\boldsymbol{n}$ points along one of the edges of the rectangular simulation cell [48]. For this reason an external field was applied in the cooling run, to reorient $\boldsymbol{n}$ (during the equilibration period) along the z direction of the simulation cell [20], when an orientationally ordered phase was first discovered. In contrast, the heating runs are characterized by $\boldsymbol{n}$ pointing initially to the z direction and, due to the very slow reorientation of the director [20], there is no need to use the aligning field.

IV. RESULTS AND DISCUSSION

A. Phase behavior

Finding the exact locations of the phase transitions is difficult, and rigorous approach would necessitate calculating the free energy for all the phases [16]. In a sequential temperature series the transition temperature can be bracketed in the way described in Ref. [21]. If the system is noted to undergo a transition from phase A to phase B between the simulated temperatures T_A and T_B ($T_B>T_A$), the approximate transition temperature can be estimated as $T_{AB}=(T_A+T_B)/2$ with the error obtained as $(T_B-T_A)/2$ [21]. The following phase sequences were found for the pure GB system with $N_{GB}=1620$ and for the mixed system with $N_{GB}=1610$ and $N_{Xe}=10$, respectively,

$$\text{pure GB:}\quad \mathrm{Cr} \underset{1.23(1)}{\overset{1.31(1)}{\rightleftarrows}} \text{Sm-}A \underset{1.47(1)}{\overset{1.45(1)}{\rightleftarrows}} N \underset{1.69(1)}{\overset{1.69(1)}{\rightleftarrows}} I;$$

$$\text{with Xe solutes:}\quad \mathrm{Cr} \underset{1.23(1)}{\overset{1.29(1)}{\rightleftarrows}} \text{Sm-}A \underset{1.45(1)}{\overset{1.47(1)}{\rightleftarrows}} N \underset{1.65(1)}{\overset{1.67(1)}{\rightleftarrows}} I;$$

where the top (bottom) values are the approximate effective transition temperatures (in units of ϵ_0/k_B) for the heating (cooling) series. These results agree with those presented by de Miguel *et al.* [21], also regarding the rather large hysteresis in the Cr-Sm-A transition. The addition of xenon solutes alters the transition temperatures maximally by 0.04 reduced units. Hence, the phase behavior is practically unaltered by the presence of xenon.

To identify the different phases, a number of order parameters were calculated. The orientational order parameter P_2 [20] can be used to distinguish between isotropic and nematic phases. It is the unique eigenvalue of the orientational ordering tensor $\boldsymbol{Q}$, with the Cartesian components

$$Q_{\alpha\beta}=\tfrac{1}{2}\langle 3\hat{u}_\alpha\hat{u}_\beta-\delta_{\alpha\beta}\rangle, \tag{18}$$

the corresponding eigenvector of which is associated with the director $\boldsymbol{n}$ of the LC phase. P_2 obtains nonvanishing values in phases possessing orientational order. For distinguishing between the N and Sm-A phases, the translational order parameter τ_1 [20] was calculated. τ_1 vanishes in phases with no long-range translational order and its nonzero value indicates the existence of a layer structure or a density wave in the system. Finally, the bulk bond orientational order parameter ψ_6 can be used to differentiate between the Sm-A and Sm-B/Cr phases. While ψ_6 is zero in the absence of intralayer order, this parameter obtains the maximum value of one when a perfect hexagonal order exists in the system. Detailed description of the calculation of these order parameters from the simulations can be found in Refs. [20,21].

Figure 3 presents the simulated order parameters P_2, τ_1, and ψ_6, as well as the average number density ρ for the mixed system with $N_{GB}=1610$ and $N_{Xe}=10$.

Panel (a) reveals discontinuities between the temperatures $T^\star=1.66$ and 1.68, $T^\star=1.46$ and 1.48, as well as $T^\star=1.28$ and 1.3 for the order parameters P_2, τ_1, and ψ_6, respectively. These mark the corresponding N-I, Sm-A-N, and Cr-Sm-A phase transitions in the heating sequence. In Fig. 3(b), the

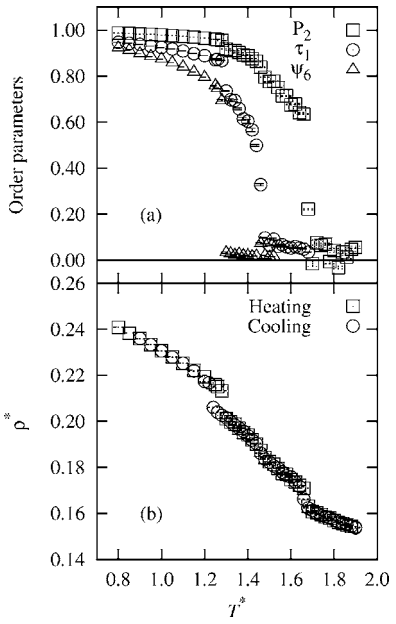

FIG. 3. (a) Simulated order parameters for the Gay-Berne model with xenon solutes, in the heating series: The orientational order parameter P_2; the translational order parameter τ_1, and bulk bond orientational order parameter ψ_6. (b) The temperature dependence of the average number density ρ.

average number density is discontinuous at the Cr-Sm-*A* and *N*-*I* phase transitions. At the Sm-*A*-*N* transition the jump in density is much less pronounced. These features are reflected in the NMR properties of the dissolved xenon (*vide infra*), which are sensitive to the density of the medium. The large hysteresis at the Cr-Sm-*A* transition is clearly visible in the temperature profile of ρ. These data are in agreement with those of a pure GB system reported in a previous study [21].

B. Structural properties

To study the effects of xenon solutes on the structure of the LC phases, the pair correlation function $g(r^\star)$ for the GB particles was calculated at temperatures well within the range of all the four phases: at $T^\star=1.15$ (Cr), 1.38 (Sm-*A*), 1.6 (*N*), and 1.8 (*I*). This was done for both the pure GB system and the one with the xenon solutes. Practically no changes were observed between these two types of systems. Compared to the $g(r^\star)$ presented by Bates and Luckhurst [20], an almost perfect agreement was found for the three liquid phases *I*, *N*, and Sm-*A*. In contrast, the low-temperature phase showed a substantially more ordered structure than in Ref. [20]. de Miguel *et al.* [21] calculated various intralayer and interlayer correlation functions which implied that the phase is better designated as Cr than Sm-*B*, due to the presence of significant interlayer order. In the present paper the focus is on Xe NMR in the three high-temperature phases of the model, and we adopt the phase designation of de Miguel *et al.*

From the viewpoint of the NMR experiments, an interesting question is how the xenon solutes are located with respect to the solvent molecules. To study this, pair correlation function between xenon solutes and GB particles was calculated at the above-mentioned four temperatures. The results are displayed in Fig. 4. The pair correlation functions for the *I* and *N* phases [Figs. 4(d) and 4(c), respectively] are very similar. The location of the nearest neighbor peak at $r^\star \approx 1.0$ reveals that the Xe solutes have a slight preference of residing in the side configuration with respect to the GB particles, in these phases with no translational order. The smaller peak at $r^\star \approx 2.0$ corresponds to the next nearest neighbors. In the Sm-*A* phase the pair correlation function, Fig. 4(b), shows more structure. In addition to the nearest neighbor peak at 1.0 there are also comparably high peaks around $r^\star=2.0$ and $r^\star=3.0$, implying above-average concentration of xenon solutes located close to the "tail" areas of

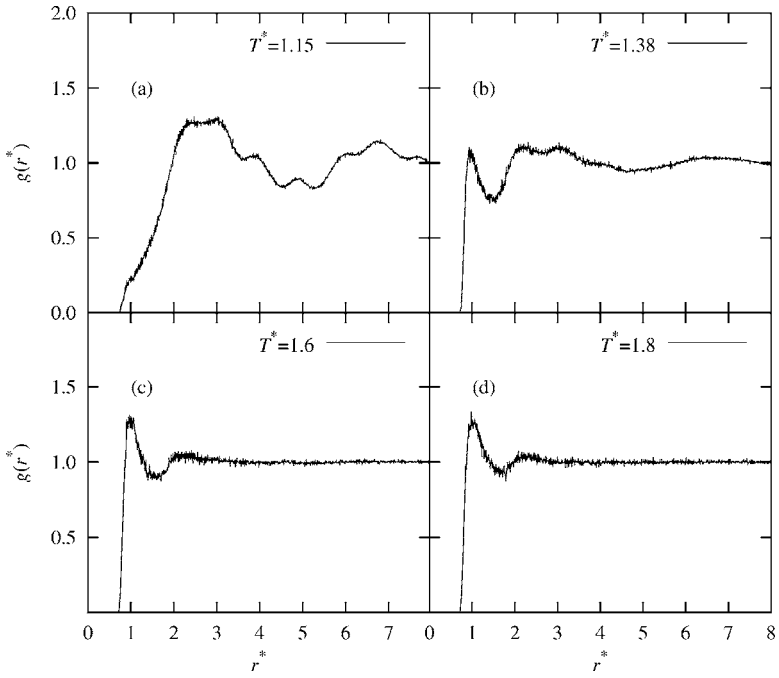

FIG. 4. Pair correlation functions $g(r)$ between Gay-Berne particles and xenon solutes in the different phases of the model: (a) Molecular crystal ($T^\star=1.15$), (b) smectic-*A* liquid crystal ($T^\star=1.38$), (c) nematic liquid crystal ($T^\star=1.6$), and (d) isotropic liquid ($T^\star=1.8$).

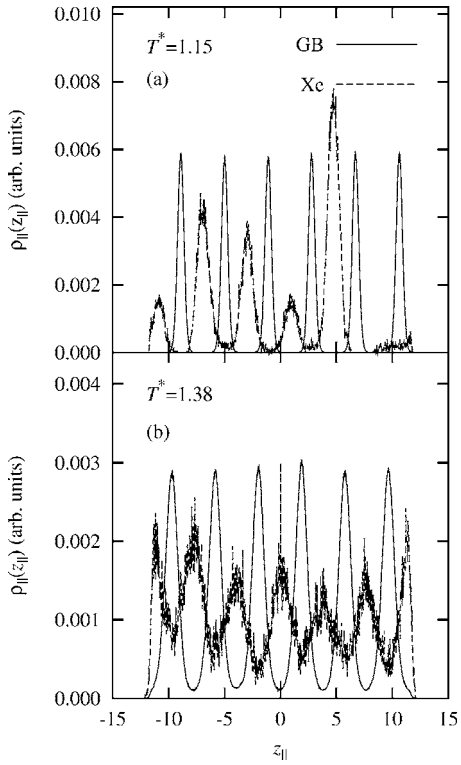

FIG. 5. One-body density distribution along the director of the phase for Gay-Berne particles and xenon solutes in (a) molecular crystal ($T^\star=1.15$) and (b) smectic-A liquid crystal ($T^\star=1.38$) phases.

the GB molecules. In the Cr phase, $g(r)$ has its nearest neighbor peak approximately at the scaled distance of 2.0, with a plateau of almost constant values up to $r^\star \approx 3.0$, as evident from Fig. 4(a). This indicates that in the Cr phase there are hardly any xenon solutes in the side configuration with respect to the GB particles, i.e., the solutes are expelled from the highly ordered molecular layers. The correlation function also shows the persistence of order to larger distances than in the other phases of the model.

To further study the location of the xenon solutes with respect to the layers formed by GB particles, the one-body (singlet) translational distribution functions $\rho(z_\|^\star)$ were calculated both for GB particles and Xe guests in the Sm-A and Cr phases. The reduced coordinate $z_\|^\star$ is measured along the director of the phase, i.e., perpendicular to the molecular layers. From Fig. 5(b) for the Sm-A phase, it is evident that the solutes prefer interlayer position in this translationally ordered LC phase. However, an overlap in the Xe and GB particle distributions exists, indicating that there are Xe atoms inside the molecular layers, too. This is in agreement with the nearest neighbor peak at $r^\star \approx 1.0$ in the pair correlation function, Fig. 4(b), for Sm-A phase. The ratio of the interlayer Xe density maxima to the intralayer minima is about 3…4. In contrast, theoretical analysis of experimental Xe NMR data in Ref. [24] suggests a much less pronounced expulsion of the Xe solutes from the molecular layers in the smectic phases: the density of xenon in the interlayer space was found to only exceed that of the intralayer region by a few percent [52]. While this finding is a result of a theoretical model applied to experimental data [24], the most likely reason for the discrepancy is in our rigid GB model. We would expect increased intralayer penetration of the xenon solutes if the LC molecules were represented by a more realistic model where flexible molecular tails are introduced [53].

In agreement with the interpretation of the GB-Xe pair correlation function, the singlet distribution functions in the Cr phase, Fig. 5(a), show virtually no penetration of Xe into the molecular layers. The peaks are higher and narrower which indicates decreased deviation from the layer centers.

C. Nuclear magnetic resonance parameters

1. Analysis

With the magnetic field of the NMR spectrometer in the z direction of the laboratory frame, the thermal average observable $\langle T_{zz}\rangle$ corresponding to a general two-index interaction tensor $\boldsymbol{T}$ can be decomposed into isotropic and anisotropic contributions as [4]

$$\langle T_{zz}\rangle = T^{\mathrm{iso}} + T^{\mathrm{aniso}} = \frac{1}{3}\sum_{\alpha}\langle T_{\alpha\alpha}\rangle + \frac{2}{3}\sum_{\alpha\beta}\langle s_{\alpha\beta}T_{\alpha\beta}\rangle, \quad (19)$$

where α,β are Cartesian coordinates in some conveniently chosen molecule-fixed frame.

$\boldsymbol{T}$ is in the present case either the $^{129/131}$Xe shielding tensor or ^{131}Xe quadrupole coupling tensor. With a macroscopic number of LC molecules appropriate to experimental conditions, the director $\boldsymbol{n}$ of the phase either coincides with or is perpendicular to the magnetic field $\boldsymbol{B}_0$, depending on the type of LC [4]. We treat the former case but note that comparison with experiments carried out for the latter type of LCs is facilitated by multiplying T^{aniso} by the factor of $-1/2$. In a simulation sample, however, the unique principal axis of the instantaneous orientational ordering tensor $\boldsymbol{Q}^{\mathrm{inst}}$ fluctuates slightly from a snapshot to another and does not stay exactly aligned with the laboratory z axis. To reduce the amount of numerical noise arising from this finite size effect, the pairwise GB-Xe and Xe-Xe interaction contributions to the NMR property tensors are transformed to and averaged in the principal axis frame of $\boldsymbol{Q}^{\mathrm{inst}}$ (with $\boldsymbol{n}^{\mathrm{inst}}$ coinciding each time with $\hat{z}$), for each simulation snapshot. The background for this is discussed in the auxiliary material [26]. The α,β in the transformation of Eq. (19) are chosen to denote the Cartesian coordinates in the local GB-Xe or Xe-Xe interaction frames of Fig. 1. Averaging over snapshots is carried out subsequently.

The isotropic part σ^{iso} is the shielding constant, whereas the traceless $\boldsymbol{\chi}$ tensor lacks the corresponding contribution, and by quadrupole coupling *constant*, the principal value of $\boldsymbol{\chi}$ with the largest absolute value is meant instead. The formula for the anisotropic part T^{aniso} involves the tensor

$$s_{\alpha\beta} = \tfrac{1}{2}(3\cos\theta_{\alpha z}\cos\theta_{\beta z} - \delta_{\alpha\beta}) \quad (20)$$

that is related through time and/or ensemble averaging to the traceless and symmetric Saupe orientation tensor, $S_{\alpha\beta} = \langle s_{\alpha\beta}\rangle$ [54]. Based on the above, S_{zz} coincides with the orientational order parameter P_2 [Fig. 3(a)], and $\theta_{\alpha z}$ are the

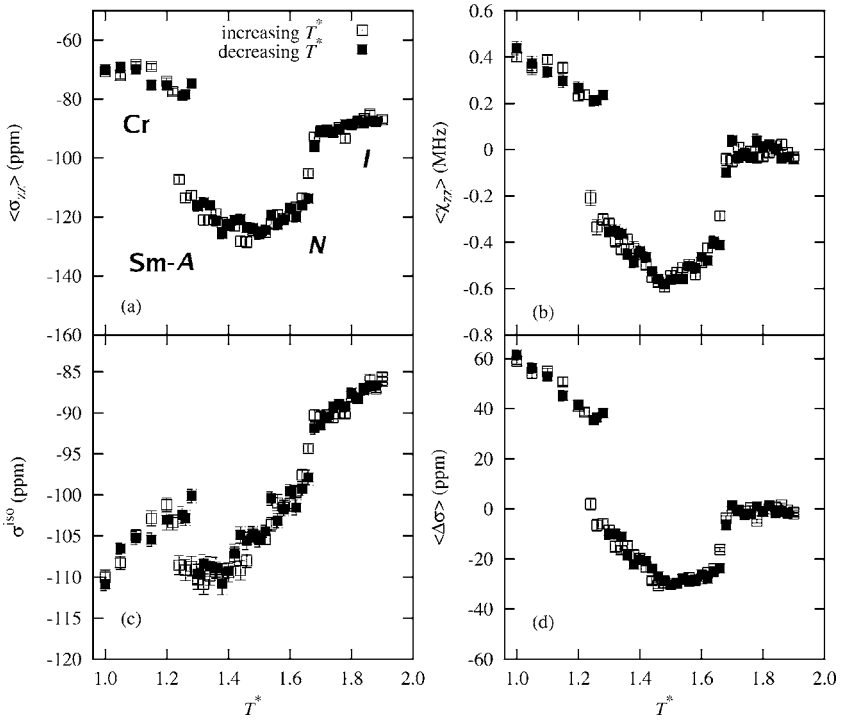

FIG. 6. Simulated temperature evolution of the nuclear magnetic resonance parameters of atomic xenon dissolved in Gay-Berne model liquid crystal: The measurable (a) $^{129/131}$Xe nuclear shielding $\langle\sigma_{zz}\rangle$ relative to the free atom and (b) ^{131}Xe quadrupole coupling $\langle\chi_{zz}\rangle$; the breakdown of observable shielding to (c) isotropic shielding constant σ^{iso}, and (d) shielding anisotropy $\langle\Delta\sigma\rangle$. The different phases are indicated in panel (a).

angles between the axes of the pair interaction frame and the magnetic field.

We investigate uniaxial LC phases with cylindrically symmetric physical properties around $\boldsymbol{n}$. If one further assumes that the orientation of the interacting GB-Xe or Xe-Xe pairs with respect to $\boldsymbol{B}_0$ and the magnitude of the NMR interactions $T_{\alpha\beta}$ are statistically uncorrelated, i.e., $\langle s_{\alpha\beta}T_{\alpha\beta}\rangle \approx S_{\alpha\beta}\langle T_{\alpha\beta}\rangle$, one arrives at a further simplification of the anisotropic contribution to $\langle T_{zz}\rangle$,

$$T^{\mathrm{aniso}} \approx \tfrac{2}{3}P_2\langle\Delta T\rangle, \tag{21}$$

where the anisotropy of $\boldsymbol{T}$ is defined as

$$\Delta T = T_{zz} - \tfrac{1}{2}(T_{xx} + T_{yy}). \tag{22}$$

The temperature evolution of $\langle T_{zz}\rangle$ in the different LC phases is seen to be determined by the average T^{iso} as well as (in the anisotropic phases with $P_2 \neq 0$) $\langle\Delta T\rangle$ and P_2. We calculate in the analysis of the simulation data the σ^{iso} and T^{aniso} (with $T=\sigma,\chi$) using the full definition in Eq. (19). For additional analysis, $\langle\Delta\sigma\rangle$ is separately calculated using, for T_{xx} and T_{yy}, the analogs of $s_{\alpha\beta}$ in Eq. (20) where the respective angles $\theta_{\alpha x}$ and $\theta_{\alpha y}$ refer to the two eigenvectors of $\boldsymbol{Q}^{\mathrm{inst}}$ that are perpendicular to $\boldsymbol{n}^{\mathrm{inst}}$. We note that the concept of anisotropy is not necessary for the traceless quadrupole coupling tensor, as $\Delta\chi = \frac{3}{2}\chi_{zz}$.

The estimates of statistical errors were performed by the "blocking" method described by Flyvbjerg and Petersen [55]. The method involves consecutive halving of the amount of data where at each step two adjacent data points are averaged to give a new data point for the next round, producing a one-half as large data set. The statistical correlation contained in the data decreases with the number n of transformations and, consequently, error estimates are improved in the process. The proper error bar is selected from the plateau observed as a function of n.

The measurable NMR quantities $\langle\sigma_{zz}\rangle$ (with respect to the free Xe atom) and $\langle\chi_{zz}\rangle$, as well as σ^{iso} and $\langle\Delta\sigma\rangle$ that represent the breakdown of the observable shielding to isotropic and anisotropic contributions, respectively, are presented as functions of temperature in Fig. 6. The simulated properties of Xe shielding [Figs. 6(a), 6(c), and 6(d)] as a function of decreasing temperature and in the *I*-*N*-Sm-*A*-Cr succession of phases may be compared to the ^{129}Xe and ^{21}Ne NMR experiments carried out for the NCB 84 [1-butyl-*c*-4-(4′-octylbiphenyl-4-yl)-*r*-1-cyclo-hexan-carbonitrile] LC [24] as well as reflected against the prevailing phenomenological models [24,56,57].

A noteworthy aspect of the quantum chemical results for Xe shielding when interacting with other atoms or molecules, is that practically all the dependence on the environment comes from the changes in the negative, paramagnetic contribution, which arises through excited electronic states and vanishes for the free atom [27]. The introduction of neighboring molecules can be viewed as causing an increase in the density of such states and, consequently, a deshielding influence. This is reflected in the characteristic direction of the ^{129}Xe chemical shift in different liquids [58] and LCs [4], as well as in the present simulations, where ^{129}Xe shielding is always lower than that of the free atom.

2. Shielding in the isotropic phase

The interpretation involving the density of excited states is consistent also with the phenomenological supposition that the interaction contributions to Xe shielding in liquids should be proportional to the local *number density* of the neighboring solvent molecules [24,56]. Liquids typically exhibit lin-

ear dependence of the density on temperature, and this is also the case for the present GB model, as evident from Fig. 3(b). Indeed, experimentally the isotropic phase of LC systems is characterized by a linear $\langle\sigma_{zz}\rangle$ vs temperature curve.

In NCB 84, the xenon shielding becomes less negative by 0.183 ppm/K with increasing T [24]. We find qualitatively the same behavior in the simulated σ^{iso}. In our case we cannot base estimates of the slope on the temperature scale furnished by the reduced unit $\Delta T^{\star}=\epsilon_0/k_B\approx 1800$ K, as this leads to mesophases existing at an unrealistically high temperature range (e.g., melting point beyond 2300 K in our parametrization). Instead, a more realistic comparison where this deficiency of the GB model has been reduced, assigns the widths of the simulated temperature ranges where the Sm-A and N phases exist, 0.20 and 0.23 $\Delta T^{\star}$ (averaging the results of both ascending and descending temperature series), with the experimental [59] values for NCB 84, 16.7 K and 30.1 K, respectively. Based on the average of these two ranges, $\Delta T^{\star}$ corresponds to 107 K and the slope of the simulated linear temperature dependence [Fig. 6(c)] of σ^{iso} equals roughly 0.3 ppm/K, in agreement with the experiment. The linear temperature dependence is less apparent in the simulated total shielding $\langle\sigma_{zz}\rangle$ [Fig. 6(a)] due to the numerical fluctuation of the anisotropic part around zero value appropriate to the I phase. The noise is due to finite size effects both on the order parameter P_2 [Fig. 3(a)] and the shielding anisotropy $\langle\Delta\sigma\rangle$ [Fig. 6(d)], the product of which σ^{aniso} is proportional to, according to Eq. (21).

The simulated NMR data result from a delicate balance of the anisotropic forces between the mesogens and the xenon solute, as well as the associated NMR interactions. These two have different dependence on the separation of the interacting pair. The fact that the level of the simulated isotropic shielding is around −90 ppm in contrast to the experimental −182 ppm in NCB 84 [24], implies an overall reduced NMR interaction in the simulation as compared to the NMR measurement. This might be caused by a too repulsive GB-Xe potential, keeping the solutes at slightly too large distances from the solvent molecules and, hence, effectively limiting the overlap-dominated NMR interactions that decay rapidly with the separation. However, our careful procedure of determining the rotationally averaged GB-Xe potential with counterpoise-corrected RI-MP2 calculations is likely to, if anything, lead to a too *attractive* interaction. Underestimated strength of the NMR shielding parameters (Table II) could also cause a too small σ^{iso}, but the fact that strong simulated phase transition effects (*vide infra*) are associated with the onset and temperature evolution of σ^{aniso}, which is determined by the same parametrized tensor components of $\boldsymbol{\sigma}-\boldsymbol{\sigma}_{\mathrm{free}}$ as the isotropic part, does not point to this conclusion. Instead, one is led to doubt that the rigidity of the GB model, well suited for the core region of the mesogen but less appropriate to the flexible tails, may limit the access of xenon to the range of strongest NMR interaction with the solvent.

3. Shielding in the nematic phase

At the N-I phase transition, the anisotropic contribution to $\langle\sigma_{zz}\rangle$ sets in and an abrupt jump of the shielding to values some 20 ppm lower than in the I phase, is observed in the simulation [Fig. 6(a)]. This is in qualitative agreement with Xe NMR experiments, e.g., for NCB 84 [24]. The jump in σ^{aniso} results from two effects: on the one hand the electron cloud of the xenon solute in an isotropic liquid retains on the average the spherical shape appropriate to a free Xe atom, but experiences an axial deformation along $\boldsymbol{n}$ in the mesophases. This is reflected in the vanishing or nonvanishing value of $\langle\Delta\sigma(I/N)\rangle$. On the other hand, even a nonzero $\langle\Delta\sigma\rangle$ such as that commonly occurring in molecules, would not be observable in the I phase because the anisotropic part of the observable is proportional to the product of the orientational order parameter and the anisotropy, $P_2\langle\Delta\sigma\rangle$ [as in Eq. (21)], and P_2 jumps to nonzero values when the temperature decreases below that of the N-I transition. From Fig. 6(d) we find that the simulated value of $\langle\Delta\sigma\rangle$ is ca. −27 ppm in the N phase. This quantity has the correct sign but has 2…3 times larger magnitude than the characteristic results in thermotropic LCs [60].

The experimentally observed discontinuity of ^{129}Xe shielding at the N-I phase transition in NCB 84 equals 4.9 ppm [24]. We thus find that whereas our simulation reproduces the direction of the jump, its magnitude is overestimated in the model. The values of the orientational order parameter P_2 obtained in the GB model compare very well with those observed in the N phase of thermotropic LCs. With P_2 increasing rapidly from zero to about 0.65 when entering the N phase, Eq. (21) with $\langle\Delta\sigma\rangle\approx -27$ ppm predicts a jump of σ^{aniso} to a bit less that 10 ppm in the deshielding direction. The overestimated discontinuity in σ^{aniso} in our model results partially from the exaggerated $\langle\Delta\sigma\rangle$ in the N phase.

As evidenced by panel (c) of Fig. 6, not only σ^{aniso} but also σ^{iso} experiences a sudden deshielding change of ca. 5 ppm. According to phenomenological models [24,56], both σ^{iso} and σ^{aniso} are associated with the medium density, which, in the present parametrization of the GB model, increases abruptly by about 4% when entering the more ordered N phase from the I phase, as visualized in Fig. 3(b). Attributed as a characteristic deficiency of the GB model [20], such a change may be exaggerated by one order of magnitude in GB simulations as compared to typical real LCs, e.g., 0.5% [59]. Most likely the overestimated magnitude of the discontinuity in ρ is one important factor behind the lack of quantitative agreement of the magnitude of the discontinuity in Xe shielding at the N-I transition with experiment.

In the N phase, the simulated absolute value of the shielding anisotropy is approximately a linearly decreasing function of temperature [Fig. 6(d)], but the order parameter P_2 follows a strongly nonlinear temperature dependence, in particular close to the phase transition [Fig. 3(a)]. Consequently, the resulting σ^{aniso} is also nonlinear, in agreement with both the experiment [24] and phenomenological theories [24,56,57]. The total change of ^{129}Xe shielding in the N phase amounts to ca. 13 ppm in the simulation [Fig. 6(a)] and 8 ppm in the experiment. The improved relative performance of the model in this respect, as compared to the magnitude of the discontinuity at the N-I transition, lends support

for our supposition that the overestimated density jump is mainly responsible for the large discontinuity.

4. Shielding in the smectic-A and molecular crystal phases

The simulation results indicate virtually no discontinuity, but instead a change in the slope and trend in $\langle\sigma_{zz}\rangle$ at the Sm-*A*-*N* transition. This is again in complete qualitative agreement with the experimental findings [24]. Upon decreasing temperature the Xe shielding starts to increase rapidly towards the more shielded direction, i.e., smaller interaction-induced contributions. This is consistent with the tendency of the solutes to prefer the less dense regions between the molecular layers formed in the Sm-*A* phase. However, whereas the experimental increase amounts to only 1 ppm [24], the simulated $\langle\sigma_{zz}\rangle$ rises by around 10 ppm due to parallel changes in σ^{iso} (25%) and σ^{aniso} (75%). The apparent disagreement of the magnitude is consistent with the large degree of expulsion of xenon from the smectic layers as discussed above in reference to Fig. 5(b).

The Cr-Sm-*A* phase transition is again characterized by a large discontinuity of $\langle\sigma_{zz}\rangle$, with the shielding in the former phase exceeding the latter by ca. 30 ppm in the simulation and by 9 ppm in the NCB 84 experiment [24], albeit the transition is between the Cr and Sm-*G* phases in NCB 84. The associated change of the medium density in the simulation is large, and particularly the local density around the Xe solutes changes very substantially due to the practically complete lack of overlap of the distributions of the Xe solutes and GB particles, in the Cr phase [Fig. 5(a)]. The anisotropy $\langle\Delta\sigma\rangle$ changes sign from −10 ppm in the Sm-*A* phase to +40 ppm in Cr. Interestingly, the temperature dependencies of σ^{iso} and $\langle\Delta\sigma\rangle$ (and, consequently, σ^{aniso}) are exactly the opposite in the Cr phase. The authors are not aware of any phenomenological theory for Xe shielding in Cr.

5. Quadrupole coupling

In general the simulated data for the ^{131}Xe quadrupole coupling, Fig. 6(b), are slightly noisier than for shielding. This fact is associated with the even steeper decay with distance of $\boldsymbol{\chi}$ than that of $\boldsymbol{\sigma}$, and the consequently poorer statistics.

The simulated temperature dependence of $\langle\chi_{zz}\rangle$ follows closely that of σ^{aniso}, due to the similar dependence of these two quantities on P_2. $\langle\chi_{zz}\rangle$ fluctuates around the appropriate value of zero in the *I* phase, and experiences a jump to finite values at the *N*-*I* phase transition, in agreement with the findings for ^{21}Ne in NCB 84 [24]. In the experiment, $\langle\chi_{zz}(^{21}\mathrm{Ne})\rangle$ is first positive, but changes sign and continues to grow more negative upon decreasing temperature in the *N* phase and beyond. Our data for ^{131}Xe are consistently negative in the Sm-*A* and *N* phases, and 2…3 times overestimated in magnitude as compared to the typical experimental data in nematics around 150, …, 180 kHz [25]. Experimentally a local maximum in $|\langle\chi_{zz}\rangle|$ is often seen in ^{21}Ne, ^{83}Kr, and ^{131}Xe NMR in the *N* phase [24,25], but this cannot be extracted from the current simulation.

It is noteworthy that the phenomenological model of Ref. [24] for $\langle\chi_{zz}\rangle$ involves both the electric field gradient (EFG) at the nuclear position due to the deformation of the electron cloud (induced by anisotropic intermolecular forces) and the "external" EFG due to the permanent electric dipoles of the solvent. We include the former effect but explicit electrostatic interactions are completely absent in our present simulation model. Furthermore, the parametrization with the symmetric hydrocarbon model LC molecule of Fig. 2 should ensure that also the implicit effects are absent from the parameters of the effective GB-Xe interaction. Real LC systems such as NCB 84 involve such an external EFG and, consequently, deviations between the simulated and experimental quadrupole couplings may be expected.

After a minor feature at the Sm-*A*-*N* phase transition, $\langle\chi_{zz}\rangle$ continues toward more positive values in Sm-*A* with decreasing temperature. Finally, the Cr-Sm-*A* transition is characterized by a large simulated discontinuity in $\langle\chi_{zz}\rangle$ in analogy with $\langle\sigma_{zz}\rangle$.

V. CONCLUSIONS

We have performed constant-pressure Monte Carlo simulations of the isotropic (*I*), nematic (*N*), smectic-*A* (Sm-*A*), and molecular crystal (Cr) phases of thermotropic liquid crystal (LC) solvents using the Gay-Berne model with GB(4.4,20.0,1,1) parametrization, and introduced atomic xenon solutes modeled by Lennard-Jones potentials. The solute-solvent interaction potential energy and the anisotropic nuclear magnetic resonance (NMR) observables of the solutes, $^{129/131}$Xe shielding relative to the free atom as well as ^{131}Xe quadrupole coupling, have been carefully parametrized based on first-principles quantum chemical calculations. The anisotropic NMR observables are summed in a common coordinate frame furnished by the principal axis system of the orientational order tensor, from interactions with the solvent molecules in the pairwise additive approximation.

The simulation results indicate that adding xenon solutes in an approximate experimental concentration does not significantly change the ordering or phase behavior of the LC. The xenon solutes were found to strongly prefer interlayer positions in the translationally ordered Sm-*A* and Cr phases.

Several features of experimental Xe NMR spectra as well as the existing phenomenological models are qualitatively reproduced in the simulation. In particular, the data can be interpreted in terms of the temperature dependence of the density and the orientational order parameter of the medium. The experimental shielding $\langle\sigma_{zz}\rangle$ (with the magnetic field in the *z* direction) equals the sum of σ^{iso} and the anisotropic contribution σ^{aniso}, the latter proportional to shielding anisotropy $\langle\Delta\sigma\rangle$ with respect to the director of the mesophase. The traceless quadrupole coupling tensor lacks an isotropic part, hence $\langle\chi_{zz}\rangle=\chi^{\mathrm{aniso}}$.

In the isotropic phase the anisotropic observables fluctuate around zero, and the interaction-induced contribution to σ^{iso} decreases linearly with temperature, reflecting the concurrent decrease of the density of the medium. While the slope of σ^{iso} is comparable to the experimental results, the overall magnitude of the total, negative, interaction contribution is underestimated.

At the *N-I* phase transition σ^{aniso} and $\langle\chi_{zz}\rangle$ jump to finite values due to the onset of orientational order in the *N* phase. Also σ^{iso} exhibits a discontinuity paralleling that in the density, at the phase transition. The change in the total shielding is larger than found experimentally, presumably due to the tendency of the GB model to exaggerate density changes at the *N-I* phase transition. In the *N* phase the shielding and quadrupole coupling follow the nonlinear temperature evolution of the orientational order parameter.

In agreement with the experiment, the simulated NMR observables indicate no discontinuity but a change of slope as the temperature is lowered below the Sm-*A*-*N* phase transition. The interaction-induced, negative shielding decreases in magnitude in the Sm-*A* phase, reflecting the facts that the solutes are partially expelled from the molecular layers and there is an associated decrease in the density of the local environment of the solute. The change in shielding exceeds its experimental counterpart by an order of magnitude due to the exaggerated extent of the expulsion. The quadrupole coupling follows the same trend. Finally, both shielding and quadrupole coupling exhibit a large discontinuity at the Cr-Sm-*A* phase transition.

The many qualitative successes of the present simulation model allow extensions to studies of, e.g., confined LC solutions through simulation of $^{129/131}$Xe NMR parameters, as well as the incorporation of lighter noble gas solutes, ^{3}He, ^{21}Ne, and ^{83}Kr. Nevertheless, the facts that the model suffers from an overestimated sensitivity of the NMR observables to phase transitions as compared to the available experimental data, a strong preference of the solutes to occupy interlayer positions in the translationally ordered phases, as well as the too small overall level of shielding interactions, all indicate that there is room for improvement. The most obvious direction is to reduce the degree of coarse graining in the LC model, by introduction of flexibility characteristic to the tails of real mesogens. This will presumably allow increased exposure of the solutes to the LC core regions and, consequently, increased NMR interactions, less dramatic density changes at phase transitions, and less complete expulsion of the solutes to the interlayer space in the translationally ordered phases. Work along these lines is in progress in our laboratory.

ACKNOWLEDGMENTS

The authors thank Dr. Juhani Lounila and Professor Jukka Jokisaari (University of Oulu, Finland) for useful discussions. Matti Hanni (Oulu) kindly provided the Xe-Xe NMR interaction parameters. The authors are with the Finnish Center of Excellence in Computational Molecular Science (CMS). This project was supported by a Marie Curie action, within the 6th European Community Framework Program. One of the authors (J.V.) was supported by Academy Research of Finland. Further financial support from the Emil Aaltonen Foundation is gratefully acknowledged. Computational resources were partially provided by the Center for Scientific Computing, Ltd. (CSC, Espoo, Finland).

[1] J. Jokisaari, Prog. Nucl. Magn. Reson. Spectrosc. **26**, 1 (1994).
[2] D. Raftery and B. F. Chmelka, in *NMR Basic Principles and Progress*, Vol. 30, edited by P. Diehl *et al.* (Springer, Heidelberg, 1994).
[3] C. I. Ratcliffe, Annu. Rep. NMR Spectrosc. **36**, 123 (1998).
[4] J. Jokisaari, in *NMR of Ordered Liquids*, edited by E. E. Burnell and C. A. de Lange (Kluwer, Dordrecht, 2003), pp. 109–135.
[5] W. Happer, E. Miron, S. Schaefer, D. Schreiber, W. A. van Wijngaarden, and X. Zeng, Phys. Rev. A **29**, 3092 (1984).
[6] B. M. Goodson, J. Magn. Reson. **155**, 157 (2002).
[7] C. J. Jameson and A. C. de Dios, J. Chem. Phys. **97**, 417 (1992).
[8] C. J. Jameson, A. K. Jameson, B. I. Baello, and H. Lim, J. Chem. Phys. **100**, 5965 (1994).
[9] C. J. Jameson, A. K. Jameson, B. I. Baello, and H. Lim, J. Chem. Phys. **100**, 5977 (1994).
[10] J. Kantola, J. Vaara, T. T. Rantala, and J. Jokisaari, J. Chem. Phys. **107**, 6470 (1997).
[11] F. R. Salsbury, Jr. and R. A. Harris, Mol. Phys. **94**, 307 (1998).
[12] J. Autschbach and E. Zurek, J. Phys. Chem. A **107**, 4967 (2003).
[13] A. Bagno and G. Saielli, Chem.-Eur. J. **9**, 1486 (2003).
[14] C. J. Jameson, D. N. Sears, and S. Murad, J. Chem. Phys. **121**, 9581 (2004).
[15] M. Hanni, P. Lantto, N. Runeberg, J. Jokisaari, and J. Vaara, J. Chem. Phys. **121**, 5908 (2004).
[16] D. Frenkel and B. Smit, *Understanding Molecular Simulation* (Academic, New York, 2002).
[17] M. P. Allen and D. J. Tildesley, *Computer Simulation of Liquids* (Oxford University Press, Oxford, 1987).
[18] B. J. Berne and P. Pechukas, J. Chem. Phys. **56**, 4231 (1971).
[19] J. G. Gay and B. J. Berne, J. Chem. Phys. **74**, 3316 (1981).
[20] M. A. Bates and G. R. Luckhurst, J. Chem. Phys. **110**, 7087 (1999).
[21] E. J. de Miguel, E. M. del Rio, and F. J. Blas, J. Chem. Phys. **121**, 11183 (2004).
[22] H. Fukunaga, J. Takimoto, and M. Doi, J. Chem. Phys. **120**, 7792 (2004).
[23] D. J. Cleaver, C. M. Care, M. P. Allen, and M. P. Neal, Phys. Rev. E **54**, 559 (1996).
[24] J. Lounila, O. Muenster, J. Jokisaari, and P. Diehl, J. Chem. Phys. **97**, 8977 (1992).
[25] J. Jokisaari, P. Ingman, J. Lounila, O. Pulkkinen, P. Diehl, and O. Muenster, Mol. Phys. **78**, 41 (1993).
[26] See EPAPS Document No. E-PLEEE8-75-051703 for the background of (1) the model for the NMR response of the Xe solute to pair interaction with a solvent particle, (2) graphical display of the GB-Xe interaction potential and the Xe NMR parameters, and (3) the transformation and averaging of anisotropic NMR properties. For more information on EPAPS, see http://www.aip.org/pubservs/epaps.html.

[27] At the nonrelativistic level of theory the nuclear shielding tensor has a diamagnetic and a paramagnetic contribution, which can be calculated as an expectation value from the electronic wave function and a linear response of the wave function to the magnetic field of the spectrometer, respectively (see, e.g., Ref. [28]). The diamagnetic contribution changes very little between different chemical environments, such as the LC-Xe or Xe-Xe complexes and the free Xe atom. The $\sigma_{\parallel}$ component of the paramagnetic term in the GB-Xe or Xe-Xe interactions vanishes identically in the $C_{\infty v}$ point group site symmetry due to the fact that the wave function is an eigenfunction of rotation around the molecular axis, and no coupling to the excited states occurs. Consequently, $\sigma_{\parallel}^{p} \approx 0$ and $\sigma(r) \approx 0$.

[28] P. W. Atkins and R. S. Friedman, *Molecular Quantum Mechanics*, 3rd ed. (Oxford University Press, Oxford, 1997).

[29] The atomic coordinates are available from J. Vaara upon request.

[30] A. D. Becke, J. Chem. Phys. **98**, 5648 (1993); P. J. Stephens, F. J. Devlin, C. F. Chabalowski, and M. J. Frisch, J. Phys. Chem. **98**, 11623 (1994).

[31] R. Krishnan, J. S. Binkley, R. Seeger, and J. A. Pople, J. Chem. Phys. **72**, 650 (1980); T. Clark, J. Chandrasekhar, and P. v. R. Schleyer, J. Comput. Chem. **4**, 294 (1983).

[32] M. J. Frisch, G. W. Trucks, H. B. Schlegel, G. E. Scuseria, M. A. Robb, J. R. Cheeseman, J. A. Montgomery, Jr., T. Vreven, K. N. Kudin, J. C. Burant, J. M. Millam, S. S. Iyengar, J. Tomasi, V. Barone, B. Mennucci, M. Cossi, G. Scalmani, N. Rega, G. A. Petersson, H. Nakatsuji, M. Hada, M. Ehara, K. Toyota, R. Fukuda, J. Hasegawa, M. Ishida, T. Nakajima, Y. Honda, O. Kitao, H. Nakai, M. Klene, X. Li, J. E. Knox, H. P. Hratchian, J. B. Cross, C. Adamo, J. Jaramillo, R. Gomperts, R. E. Stratmann, O. Yazyev, A. J. Austin, R. Cammi, C. Pomelli, J. W. Ochterski, P. Y. Ayala, K. Morokuma, G. A. Voth, P. Salvador, J. J. Dannenberg, V. G. Zakrzewski, S. Dapprich, A. D. Daniels, M. C. Strain, O. Farkas, D. K. Malick, A. D. Rabuck, K. Raghavachari, J. B. Foresman, J. V. Ortiz, Q. Cui, A. G. Baboul, S. Clifford, J. Cioslowski, B. B. Stefanov, G. Liu, A. Liashenko, P. Piskorz, I. Komaromi, R. L. Martin, D. J. Fox, T. Keith, M. A. Al-Laham, C. Y. Peng, A. Nanayakkara, M. Challacombe, P. M. W. Gill, B. Johnson, W. Chen, M. W. Wong, C. Gonzalez, and J. A. Pople GAUSSIAN03, Revision C.02, Gaussian, Inc., Wallingford, CT, 2004.

[33] F. Weigend and M. Häser, Theor. Chem. Acc. **97**, 331 (1997); F. Weigend, M. Häser, H. Patzelt, and R. Ahlrichs, Chem. Phys. Lett. **294**, 143 (1998); C. Hättig, A. Hellweg, and A. Köhn, Phys. Chem. Chem. Phys. **8**, 1159 (2006).

[34] A. Schäfer, C. Huber, and R. Ahlrichs, J. Chem. Phys. **100**, 5829 (1994).

[35] Turbomole, Version 5.71, R. Ahlrichs, M. Bär, M. Häser, H. Horn, and C. Kölmel, Chem. Phys. Lett. **672**, 165 (1989).

[36] A. Nicklass, M. Dolg, H. Stoll, and H. Preuss, J. Chem. Phys. **102**, 8942 (1995).

[37] S. F. Boys and F. Bernardi, Mol. Phys. **19**, 553 (1970).

[38] G. R. Luckhurst and P. S. J. Simmonds, Mol. Phys. **80**, 233 (1993).

[39] Practically identical values were also obtained from the fit to the Gay-Berne potential form.

[40] WebElements,™ www.webelements.com

[41] F. J. Adrian, J. Chem. Phys. **120**, 8469 (2004).

[42] M. Straka and J. Vaara, J. Phys. Chem. A **110**, 12338 (2006).

[43] K. Fægri, Jr. (private communication). See http://folk.uio.no/knutf/bases/one

[44] G. D. Purvis III and R. J. Bartlett, J. Chem. Phys. **76**, 1910 (1982); A. C. Scheiner, G. E. Scuseria, J. E. Rice, T. J. Lee, and H. F. Schaefer III, *ibid.* **87**, 5361 (1987); J. Gauss and J. F. Stanton, *ibid.* **102**, 251 (1995).

[45] J. Lintuvuori, M.Sc. thesis, University of Helsinki, 2006.

[46] H. F. King, J. Chem. Phys. **57**, 1837 (1972).

[47] G. R. Luckhurst, R. A. Stephens, and R. W. Phippen, Liq. Cryst. **8**, 451 (1990).

[48] R. Hashim, G. R. Luckhurst, and S. Romano, J. Chem. Soc., Faraday Trans. **91**, 2141 (1995).

[49] L. Verlet, Phys. Rev. **159**, 98 (1967).

[50] P. Scharlin, R. Battino, E. Silla, I. Tunon, and J. Pascual-Ahuir, Pure Appl. Chem. **70**, 1895 (1998).

[51] M. Matsumoto and T. Nishimura, ACM Trans. Model. Comput. Simul. **8**, 3 (1998). See also http://www.math.sci.hiroshima-u.ac.jp/~m-mat/MT/emt.html

[52] J. Lounila (private communication).

[53] C. McBride and M. R. Wilson, Mol. Phys. **97**, 511 (1999).

[54] A. Saupe, Z. Naturforsch. A **19A**, 161 (1964).

[55] H. Flyvbjerg and H. G. Petersen, J. Chem. Phys. **91**, 461 (1989).

[56] M. Ylihautala, J. Lounila, and J. Jokisaari, J. Chem. Phys. **110**, 6381 (1999).

[57] M. Ylihautala, J. Lounila, and J. Jokisaari, Chem. Phys. Lett. **301**, 153 (1999).

[58] K. W. Miller, N. V. Reo, A. J. M. Schoot Uiterkamp, D. P. Stengle, T. R. Stengle, and K. L. Williamson, Proc. Natl. Acad. Sci. U.S.A. **78**, 4946 (1981).

[59] R. Kiefer and G. Baur, Liq. Cryst. **7**, 739 (1990).

[60] O. Muenster, J. Jokisaari, and P. Diehl, Mol. Cryst. Liq. Cryst. **206**, 179 (1991).